LAWRENCE
LIVERMORE
NATIONAL
LABORATORY

LLNL-JRNL-643967

Enhanced Gas Adsorption on Graphitic Substrates via Defects and Local Curvature: A Density Functional Theory Study

D. Dutta, B. Wood, S. Bhide, K. G. Ayappa, S. Narasimhan

September 19, 2013

Journal of Physical Chemistry C

Disclaimer

Enhanced Gas Adsorption on Graphitic Substrates via Defects and Local Curvature: A Density Functional Theory Study

Debosruti Dutta[1,2], Brandon C. Wood[3,4], Shreyas Y. Bhide[1], K. Ganapathy Ayappa[1], and Shobhana Narasimhan[3]
[1] *Department of Chemical Engineering, Indian Institute of Science, Bangalore 560012, India*
[2] *Department of Chemical & Biomedical Engineering, University of South Florida, Tampa, FL 33620, USA*
[3] *Theoretical Sciences Unit, Jawaharlal Nehru Centre for Advanced Scientific Research, Jakkur, Bangalore 560064, India*
[4] *Quantum Simulations Group, Lawrence Livermore National Laboratory, Livermore, CA 94550, USA*

Using van der Waals-corrected density functional theory calculations, we explore the possibility of engineering the local structure and morphology of high surface-area graphene-derived materials to improve the uptake of methane and carbon dioxide for gas storage and capture. We test the sensitivity of the gas adsorption energy to the introduction of native point defects, curvature and the application of strain. The most significant enhancements occur at concavely curved surfaces and Stone-Wales defects. Trends for CO_2 and CH_4 are similar, though CO_2 binding is generally stronger by ∼4–5 kJ mol^{-1}. However, the differential between the adsorption of CH_4 and CO_2 is exceptionally high on folded graphene sheets and at concave curvatures; this could possibly be leveraged for CH_4/CO_2 flow separation.

I. INTRODUCTION

Due to the anticipated shortage of petroleum, as well as the adverse environmental impact of conventional gasoline vehicles, alternative transportation systems based on hydrogen or natural gas are being actively researched. Since cryogenic storage is expensive and compressed gas storage is energy intensive with associated safety factors, the search is on for suitable materials that can store gas adsorptively. Carbon dioxide capture is motivated by the pressing need to reduce greenhouse gases. Enriching the methane content in a gas mixture of carbon dioxide and methane is important in enhanced oil recovery, biogas production and natural gas technology. The methane rich gas stream can be subsequently used in an on-board transportation system. Porous and disordered carbon-based materials are excellent adsorbents for gas storage and separation. They have been widely used due to their high specific surface area, low cost, minimal environmental impact, and good mechanical and chemical stability.[1–4]

Carbon-based adsorbents do not yet meet targets for on-board storage of hydrogen or natural gas. Efforts to further improve gas uptake in high surface-area porous carbon substrates have followed two general directions: the first approach consists of chemical modification by additives and surface functionalization; this is designed to enhance the per-site binding energy. In a previous report, we explored the effects of edges and chemical functional groups on gas adsorption on graphene;[5] we found that functional groups containing the OH moiety could increase binding with respect to unfunctionalized edges. Classical grand ensemble Monte Carlo simulations, with edge functionalized graphene nanoribbons revealed enhanced methane binding with COOH functional groups.[6] The local methane density around the functional groups was found to exceed the methane density on bare graphene as the pressure and functional group concentration is increased.[6] Specific functionalization to enhance local binding has also been used as a strategy for improving methane uptake in metal organic frameworks (MOFs).[7] A second approach consists of engineering of the pore geometry and morphology.[4,8,9] This approach aims to increase the overall number of accessible sites, as well as to improve diffusion kinetics and increase capillary action. In this work, we explore a third viable approach, namely, altering the *local* (as opposed to mesoscopic-scale) morphology and structure of the carbon lattice. We do this by introducing native point defects, such as vacancy complexes and bond rotations, as well as local strain-related effects, such as tension and surface buckling. Despite receiving attention in the context of graphene-based nanoelectronic devices,[10,11] the potential impact of this approach on adsorptive gas storage has not hitherto been systematically investigated in detail.

The precise microstructure of most porous carbons is difficult to characterize, but products tend to be largely graphitic, with significant local deviations from the ideal planar, six-membered ring structure.[12] The nature of these deviations depends on the processing and activation conditions employed, although examples include the introduction of chemical functional groups, edges, point defects, and local strain. There has been significant recent progress in the chemical and thermal processing of activated carbons, carbon aerogels, and other porous and disordered carbon-based substrates.[9,13–17] This has permitted unprecedented tunability of morphological features not only at the meso and macro scales, but also locally. In order to properly leverage these advances as part of a broader design roadmap, it is highly desirable to understand which local modifications might lead to measurable improvements in binding energetics and gas uptake.

Accordingly, we use density functional theory (DFT) calculations of gas binding on a wide variety of defective graphene-derived surfaces in order to assess which

local modifications provide the greatest adsorptive enhancement with respect to pristine graphene. We test the effects of five varieties of point defects, as well as linear and areal strain, and rippling and folding resulting from surface buckling under compression. These represent features that are commonly observed in nanoporous and mesoporous carbon frameworks,[10,18] and whose expression may be coupled to tunable processing parameters. The calculations are intended to inform experiments targeting specific processing approaches, as well as to improve the fidelity of mesoscale simulations of broader microstructural features. They may also be useful in related research fields, such as carbon-based gas sensors.

In this paper, we focus on methane and carbon dioxide adsorption. The motivation for this is twofold. First, these two gases have extraordinary technological relevance for solid-state natural gas storage and carbon capture, respectively. Second, the binding energies of CH_4 and CO_2 tend to be relatively large with respect to other small physisorbed gases of interest, notably H_2. This makes the possibility of achieving meaningful uptake enhancements via local structural changes more viable. We also compare the binding energies between CO_2 and CH_4 on the various defect structures studied. This is useful while developing separations technologies where CH_4 separation from CO_2 is the main objective.

II. COMPUTATIONAL DETAILS

We have used density functional theory (DFT) calculations to determine the fully relaxed geometries and energetics of CH_4 and CO_2 molecules adsorbed on graphene sheets with point defects, local strain or morphological defects. All DFT calculations were performed using the plane-wave Quantum-ESPRESSO code.[19] Norm-conserving pseudopotentials with a plane-wave cutoff of 80 Ry were used. To minimize spurious interactions between graphene sheets across periodic supercell images, a vacuum spacing of 20 Å was introduced along non-repeating directions. Brillouin zone sampling was performed using a $6 \times 6 \times 1$ Monkhorst-Pack k-point mesh. Marzari-Vanderbilt cold smearing[20] with a smearing width of 0.007 Ry was introduced for improved convergence and for savings in k-point density.

As physisorption dominates the interactions between the adsorbate and substrate, it is important to select a method of treating van der Waals dispersion forces adequately within a DFT framework. We have chosen to use the nonlocal van der Waals density functional (vdW-DF).[21,22] Spin-restricted DFT was used, as the formulation of the nonlocal correlation in vdW-DF is defined only for this case.[22] The revised Perdew-Burke-Ernzerhof (revPBE) functional has been used to compute the reference exchange term.[23]

The defect formation energy E_f was calculated using the formula:

$$E_f = \qquad (1)$$

For each adsorbate-substrate pair, the adsorption energy was calculated as:

$$E_{\mathrm{ads}} = -(E_{\mathrm{g+s}} - E_{\mathrm{g}} - E_{\mathrm{s}}), \qquad (2)$$

where $E_{\mathrm{g+s}}$ is the total energy of the adsorbed system, E_{g} is the total energy of the isolated gas molecule (CH_4 or CO_2), and E_{s} is the total energy of the bare substrate.

III. RESULTS AND DISCUSSION

A. Point defects

Scanning Tunneling Microscopy[24–28] and Transmission Electron Microscopy[29,30] of graphene, graphite and activated carbon reveal the presence a variety of native point defects, that could contribute to enhanced gas adsorption. These include monovacancies, divacancies, Stone-Wales defects, adatoms, and interstitial atoms. In addition to these native defects, the selective introduction of point defects represents a possible surface engineering strategy, e.g., by controlled deposition[31], crystal growth[32], ion bombardment[33], electron irradiation[34], or chemical treatment[35].

There have been several reports of enhanced binding of small molecules at point defect sites in graphene. Examples include the adsorption of O_2, CO, N_2, B_2 and H_2O on divacancies,[36] and the adsorption of CO_2 on monovacancies.[37] Meyer *et al.*[38] have imaged the kinetics and discussed the atomisitic mechanisms involved in the enhanced binding of these small gas molecules on point defects in graphitic substrates. Dissociative chemisorption of hydrogen molecules at point defect sites has also been extensively studied in the literature.[39]

We have studied the adsorption of CH_4 and CO_2 molecules on three important kinds of point defects known to exist in graphene sheets: monovacancies, divacancies and Stone-Wales defects (see Fig. 1).[18,33,38] The presence of a monovacancy leaves three carbon atoms with unsaturated dangling bonds. This causes considerable restructuring and bond formation between two of the carbon atoms, resulting in five- and nine-member rings (denoted 5–9 in the text).[26] Because the monovacancy may be further stabilized upon passivation with a hydrogen atom on the remaining unsaturated carbon,[40] we have also studied this configuration. The presence of divacancies (two adjacent missing carbon atoms) results in reorientation of the honeycomb lattice to form non-hexagonal rings. Here we consider two common divacancy reconstructions: the 5–8–5 and 555–777 defects. The Stone-Wales (SW) defect is a well-known low-energy transformation in which one of the C–C bonds is rotated by 90°. This results in a restructuring of four hexagons in the honeycomb lattice of graphene into a 55–77 configuration. All these defects studied were introduced in a $(4\sqrt{3} \times 4\sqrt{3})$ graphene unit cell (∼2% defect density).

Figures 1 and 2 show the final relaxed geometries and orientations of the CH_4 and CO_2 molecules adsorbed on

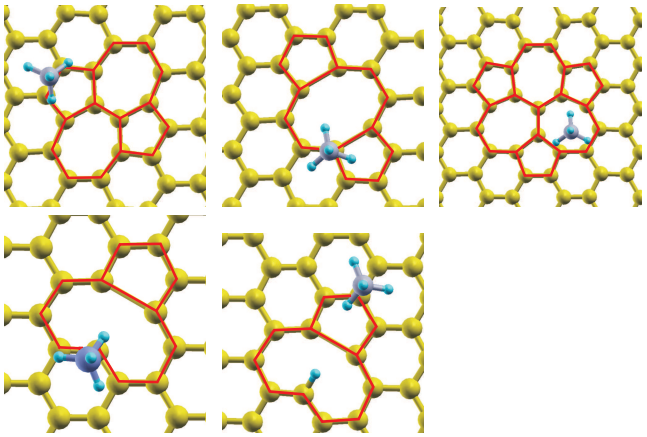

FIG. 1: (In color online) Final adsorption geometries of methane adsorbed on the tested point defects. Top row: Stone-Wales (55–77), divacancy (5–8–5), divacancy (555–777). Bottom row: monovacancy (5–9), monovacancy (5–9) with hydrogen passivation. Atomic color code – graphene C: yellow, methane C: gray, H: light blue. The red lines are guides to the eye, to bring out the bonding topology.

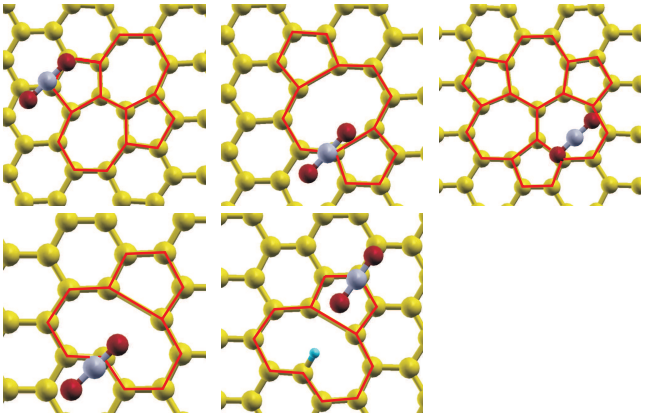

FIG. 2: (In color online) Final adsorption geometries of carbon dioxide adsorbed on the tested point defects. See Fig. 1 for defect designations. Atomic color code – graphene C: yellow, carbon dioxide C: gray, passivating H: light blue, O: maroon. The red lines are guides to the eye, to bring out the bonding topology

each of the tested point defects. For the unpassivated monovacancy defect, the CH_4 molecule sits on top of the unsaturated carbon atom in the nine-member ring such that one of its C–H bonds is oriented towards the defect site. For the 1-H passivated monovacancy defect, the CH_4 sits on the top of the carbon atom in the pentagon that is farther away from the defect site, with a geometry and orientation similar to the unpassivated monovacancy. The CH_4 molecule sits with its H-tripod down for both the 5–8–5 and 555–777 divacancy defects; however, the CH_4 molecule sits on top of the carbon atom adjoining the pentagon and octagon for the 5–8–5 defect, whereas for the 555–777 defect, CH_4 sits above a heptagon center. In the case of the SW defect, the CH_4 molecule sits on a bridge between a C–C bond that is farther away from the defect site, in one of the pentagons formed in the SW defect. For all these configurations, the CH_4 molecule sits with its tripod facing towards the substrate, at a distance of ~ 3.6 Å from the carbon atom of the methane to the graphene plane.

The adsorption sites for the CO_2 molecule on the various tested defects in the graphene sheet after geometry optimization are similar to those for CH_4 adsorption. In most cases, the linear CO_2 molecule sits at a distance of 3.5 Å, oriented parallel to the basal plane. In the case of the strongest-binding SW defect, the distance reduces to 3.35 Å, indicative of the stronger binding in this configuration.

Our results for the adsorption energies for CH_4 and CO_2 gas molecules on the monovacancy, divacancy, and SW defects, as well as the corresponding formation energies of the defect complexes, are shown in Table I. For comparison, we also present the results for adsorption on a pristine graphene sheet. From the adsorption energies, one can conclude that, in general, the greater the number of atoms that are removed from the graphene sheet to create the defect, the less favorable binding becomes, for both CH_4 and CO_2. This suggests that the symmetry breaking and rehybridization induced by the defects are competing with the possible loss of van der Waals dispersion interactions due to missing carbon atoms. We see the largest enhancement with respect to pristine graphene for the SW defect, where no carbon atoms are removed from the lattice. In this case, the presence of the non-hexagonal rings enhances binding by 23% for CH_4 and 17% for CO_2, making it by far the best candidate among those tested, for enhanced uptake of both gases. For monovacancies, the loss of a single carbon atom translates to a more modest enhancement, whereas for the divacancies, the absence of two atoms entirely offsets any gain that might otherwise be observed. Interestingly, the hydrogen passivation of a monovacancy defect slightly increases CO_2 adsorption, while decreasing CH_4 adsorption. CO_2 demonstrates consistently higher binding strength with respect to CH_4 by 4–5 kJ mol^{-1}, presumably due to the presence of a quadrupole moment. The binding energy difference between CO_2 and CH_4 is a useful indicator of the efficiency of the medium for gas separation; this value is largest for the 5–8–5 divacancy, but is not significantly enhanced with respect to the graphene baseline. The enhanced binding energy for CO_2 over methane is consistent with trends observed in finite temperature Monte Carlo simulations in carbon nanotubes[41] and porous carbons.[42]

The calculated formation energies of the point defects in Table I compare well with previously reported values in the literature,[10] and give an idea of the relative native prevalence of these defects and the ease with which they can be introduced externally. The Stone-Wales defect

TABLE I: Calculated formation energies E_f, and adsorption energies E_{ads} for methane and carbon dioxide, for point defects in a graphene sheet.

System	Cell size	Defect type	E_f (kJ mol^{-1} atom^{-1})	E_{ads} (CH_4) (kJ mol^{-1})	E_{ads} (CO_2) (kJ mol^{-1})	E_{ads} (CO_2) - E_{ads} (CH_4) (kJ mol^{-1})
Graphene	$(4\sqrt{3} \times 4\sqrt{3})$	–	–	16.9	21.4	4.5
Monovacancy	$(4\sqrt{3} \times 4\sqrt{3})$	unpassivated	731.6	18.8	21.9	3.1
	$(4\sqrt{3} \times 4\sqrt{3})$	1-H passivated	544.9	18.2	23.1	4.9
Divacancy	$(4\sqrt{3} \times 4\sqrt{3})$	5–8–5	755.5	15.9	21.1	5.2
	$(4\sqrt{3} \times 4\sqrt{3})$	555–777	676.3	16.3	20.2	3.9
Stone-Wales	$(4\sqrt{3} \times 4\sqrt{3})$	55–77	495.3	20.8	25.1	4.3

has the lowest formation energy among the tested point defects[43,44] and hence is likely to exist in relative abundance. Because it also demonstrates by far the largest adsorption strength enhancements, we conclude that a low-energy substrate treatment that causes bond reorientation without ejecting carbon atoms from the lattice would be a good potential improvement strategy. In contrast, higher-energy treatments that introduce vacancies are unlikely to lead to appreciable gas storage enhancement.

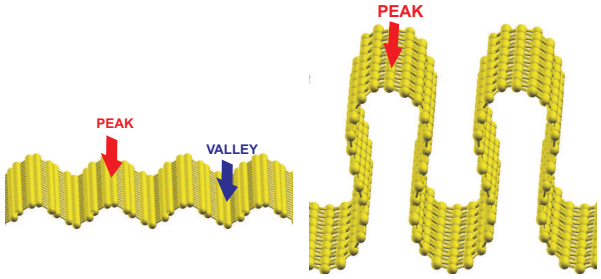

FIG. 3: (In color online) Models used for the rippled (left) and folded (right) graphene surfaces. The tested peak (convex) and valley (concave) adsorption sites are shown.

B. Local strain and morphology

Local lattice strain is inherent in amorphous systems such as nanoporous carbon, due to intrinsic stresses that arise in the planar graphene sheet from the presence of defects and altered microstructure.[18] In addition, atomic resolution imaging of graphene directly shows the presence of both small and large undulations and folds in the graphene sheet.[45–47] These local strain and morphological transformations may be exploited to increase adsorption. A similar effect has been observed in the context of strain-enhanced binding of metal atoms to graphene surfaces,[48] as well as curvature-enhanced binding of H_2 on carbon nanotubes.[49] There exists a connection between the local morphological features we discuss here, and mesostructural properties such as pore geometry; nevertheless, proper control during processing allows the local morphological features to be tuned independently.

We have examined the variation in gas adsorption energy as a function of both tensile and compressive strain. For tensile strain, both linear and areal strain were assessed, i.e., axial strain applied along one or both of the in-plane hexagonal primitive lattice vectors. Under compressive strain, we found that graphene is most likely to undergo a low-energy corrugation transformation.

1. *Ripples and Folds*

We modeled surface sheets of graphene, rippled under compressive strain via a sinusoidal variation along the zigzag direction. The undulation leads to two likely adsorption sites, which we term the peak (convex) and valley (concave) sites of a "ripple" (see Fig. 3). Both of these were tested independently.

We also tested the limiting case when the amplitude of the undulations is sufficiently large, and the curvature sufficiently strong, that a fragment of the graphene sheet folds on itself. A similar transformation has been observed experimentally.[45,50,51] We refer to this as "folded" graphene, or a "fold". In the model, the interlayer spacing at the fold center is matched to that of bulk graphite, meaning it should have properties of both single-layer rippled and bulk graphitic materials. Since the adsorption of a gas molecule in the valley site of a fold is limited by pore diffusion, we have only studied the gas adsorption at the peak (convex) site.

Our models for the rippled and folded graphene, along with the tested adsorption sites for each, are illustrated in Fig. 3. The calculated adsorption energies for CH_4 and CO_2 on each of the curved model systems are listed in Table II, and shown graphically in Fig. 4. We see that in the case of rippled graphene, gas adsorption is significantly enhanced at a valley site, but reduced at a peak site. The adsorption strength initially increases with curvature, but saturates at a compressive strain of about 10%. At 10% rippling strain, CH_4 and CO_2 adsorption at the valley site increases by 26% and 31%, respectively, over the baseline adsorption on graphene.

There are two potential reasons for the enhanced adsorption at valley sites. First, there should be a larger van der Waals interaction between the adsorbate molecule due to the increase in close-proximity carbon atoms present in the ripple sidewalls. Second, the rippling induces partial sp^2-to-sp^3 carbon rehybridization at the point of highest curvature, which changes the local electron density in the π manifold that is available for binding. From these observations, it can be concluded that the binding strength of the gas molecule is strongly dependent on the adsorption site, and that the curvature of the ripple matters up to a certain limit (∼10% compressive strain).

This is of interest not only for curved elemental carbon structures, but because the adsorption of various other atoms on a graphene sheet (such as metal adatoms, or as happens in the formation of graphene oxide) can lead to signifcant buckling of the graphene sheet, leading to increases in local curvature, thus providing concave sites that could become favored sites for gas binding. Adsorbates will therefore tend to preferentially aggregate at concave perturbations in the graphene surface. Such perturbations might also be expected at pore walls in nanoporous or disordered carbon. The final loading of the gas molecules at valley sites of corrugated graphene ripples will be determined by the competition between the inferior accessibility of valley/pore interiors and their superior thermodynamics. In other words, both kinetic and thermodynamic considerations should be taken into account when devising an effective design strategy. Note that the enhanced binding at the valley site is in agreement with earlier experiments and calculations that show that the curvature of carbon nanotubes leads to an increase in the strength of physisorption.[52,53]

According to Table II and Fig. 4, the enhancements at the valley site are larger for CO_2 than for CH_4, which leads to a difference of nearly 7 kJ mol^{-1} between CO_2 and CH_4 binding at higher curvatures. This difference could potentially be leveraged for CH_4 flow purification. In contrast, the two gases show very similar binding for the peak site.

For adsorption at the valley site on the more weakly rippled surfaces, the CH_4 molecule orients with its hydrogen tripod towards the valley. At 15–20% compressive strain, this orientation makes a transition to one in which only two hydrogen atoms point directly towards the valley. At the peak site, the tripod always orients towards the surface. CO_2 maintains a fixed geometry in which the molecule is aligned perpendicular to the fold direction, regardless of the adsorption site.

Structurally, the fold represents a combination of graphite and a tightly curved ripple.[47,54] At a folded edge, one might therefore assume that the binding energy would be similar to the peak site of the rippled sheets. This is the case for CH_4, where $E_{\text{ads}} = 12.7$ kJ mol^{-1} is near the mean value for rippled graphene. However, the binding of CO_2 ($E_{\text{ads}} = 20.5$ kJ mol^{-1}) is stronger than expected, much closer to the value for pure graphene.

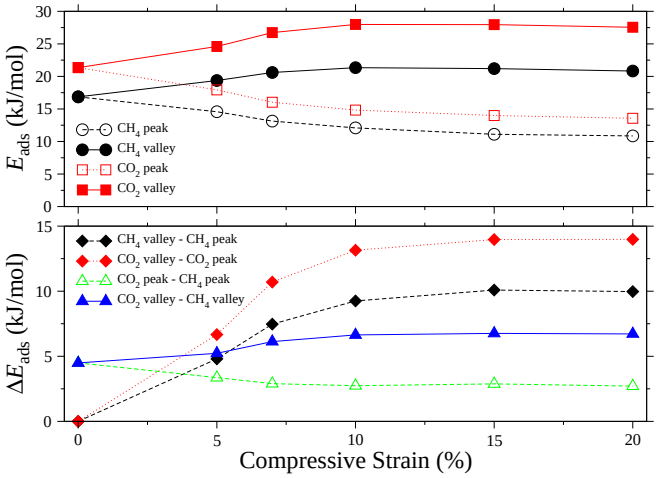

FIG. 4: (In color online) Top: Adsorption energies of CH_4 and CO_2 upon surface rippling under compressive strain. Bottom: Comparison of adsorption energies between gases and between peak (convex) and valley (concave) sites. Percent compressive strain is calculated according to $100 \times (L_0 - L)/L_0$, where L_0 and L are the initial and final supercell lengths along the rippling direction.

As a result, the difference in binding strengths between CO_2 and CH_4 is larger (8 kJ mol^{-1}) than for any other tested system. The reason for this discrepancy is not immediately clear, although it is quite possibly related to the unique electronic structure of folded graphene, where hybridization of π states between fold layers is observed.[54–56] We suggest that the fold in the graphene sheet represents a distinct species that merits further study, with potential use in the adsorptive flow separation of CH_4 from CO_2.

2. *Tensile Strain*

Our results for the adsorption energies for CH_4 and CO_2 on the systems with tensile strain are listed in Table III. We observe that the formation energies of the areal strain on graphene is roughly double than that of the linear strain. We see that the presence of in-plane linear and areal tensile strains on the graphene sheet tends to slightly decrease the binding strengths of CH_4 and CO_2. The dependence on strain is approximately linear, as shown in Fig. 5. However, the magnitude of decrease is quite small (within the range of room-temperature thermal fluctuations). We draw two conclusions from our tensile strain results: first, introducing tensile strain on the graphene sheet is not a viable engineering strategy for enhancing gas uptake; and second, the magnitude of decrease is small enough that the unintentional introduction of local tensile strain due to defect- or morphology-induced stresses will not detract appreciably from the measured absorptive capacity. The latter point is es-

TABLE II: Calculated formation energies E_f and adsorption energies $E_{\rm ads}$ of CH_4 and CO_2 for various undulations of graphene sheets. For the rippled graphene, adsorption energies for both the valley (first) and peak (second) sites are provided (see Fig. 3). Strains represent percent decreases in the linear lattice parameter.

System	Cell size	Strain magnitude	E_f (kJ mol^{-1} atom^{-1})	$E_{\rm ads}$ (CH_4) (kJ mol^{-1})	$E_{\rm ads}$ (CO_2) (kJ mol^{-1})	$E_{\rm ads}$ (CO_2) - $E_{\rm ads}$ (CH_4) (kJ mol^{-1})
Graphene	$(4\sqrt{3} \times 4\sqrt{3})$	–	–	16.9	21.4	4.5
Rippled	(4×8)	-5%	6.8	19.4 / 14.6	24.6 / 17.9	5.2 / 3.3
	(4×8)	-7%	11.6	20.6 / 13.1	26.7 / 16.0	6.1 / 2.9
	(4×8)	-10%	18.4	21.3 / 12.1	28.0 / 14.8	6.7 / 2.7
	(4×8)	-15%	29.5	21.2 / 11.1	28.0 / 14.0	6.8 / 2.9
	(4×8)	-20%	40.5	20.8 / 10.9	27.6 / 13.6	6.7 / 2.7
Fold	$(2\sqrt{3} \times 9)$	–	11.6	12.7	20.5	7.8

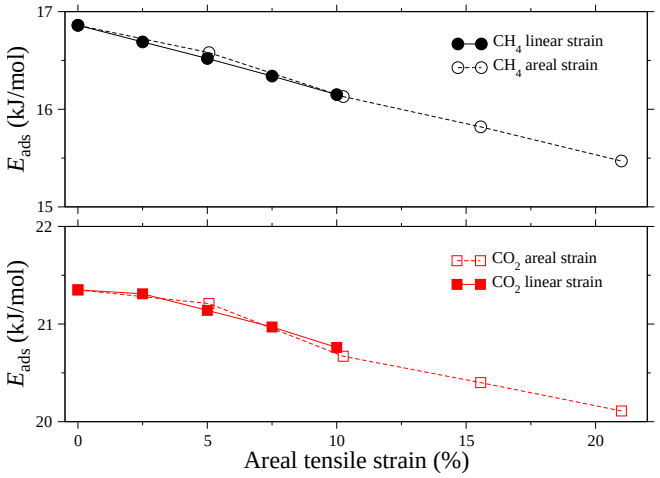

FIG. 5: Adsorption energy of CH_4 (top) and CO_2 (bottom) under tensile strain. Percent areal strain is calculated according to $100 \times (A - A_0)/A_0$, where A_0 and A are the initial and final supercell areas.

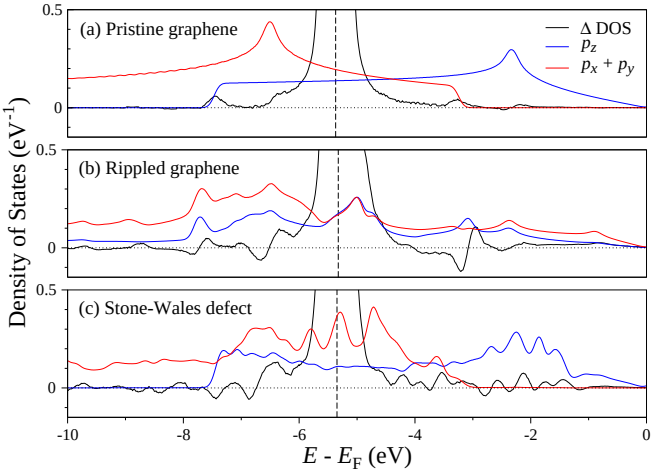

FIG. 6: (In color online) Change in the total density of states (ΔDOS) upon methane adsorption (black curve) of (a) pristine graphene, (b) rippled graphene under 20% compressive strain, and (c) graphene with a Stone-Wales defect. The blue and red curves are the projected contributions to the density of states from the p_z and $p_x + p_y$ orbitals of the carbon atom nearest to the adsorption site (taken prior to adsorption). The dashed black line is the peak position corresponding to the methane molecular level.

pecially important when considering the deliberate introduction of point defects, which may induce residual lattice strain.

C. Density of States

Some insight into the reason for enhanced binding in two of the cases — namely, the rippled graphene and the Stone-Wales defect — can be gained by examining the density of states upon adsorption, as shown in Fig. 6. Both these stronger-binding configurations demonstrate a slight degree of hybridization of the methane levels with the p orbitals of nearby carbon atoms. At the methane peak position and in the energy range of below 2 eV or so, overlap with the methane states tends to correlate with a partial mixing of p_z states with the p_x and p_y states, which is not observed in pristine graphene. The rehybridization is particularly apparent in rippled graphene, where it can be interpreted as a curvature-induced loss of sp^2 character in favor of more sp^3-like binding. Consequently, though relatively tiny, the quasi-covalent interaction with the methane enhances binding.

IV. CONCLUSIONS

In summary, we have used van der Waals-corrected density functional theory to investigate the possibility of engineering the local morphology of sp^2 carbon substrates for improved gas uptake and separation. Based on zero-temperature binding energetics, we find that the

TABLE III: Calculated formation energies E_f and adsorption energies $E_{\rm ads}$ of CH_4 and CO_2 for various strain-related transformations of graphene sheets. Strains represent percent increases in the linear lattice parameter.

System	Cell size	Strain magnitude	E_f (kJ mol^{-1} atom^{-1})	$E_{\rm ads}$ (CH_4) (kJ mol^{-1})	$E_{\rm ads}$ (CO_2) (kJ mol^{-1})	$E_{\rm ads}$ (CO_2) - $E_{\rm ads}$ (CH_4) (kJ mol^{-1})
Graphene	$(4\sqrt{3} \times 4\sqrt{3})$	–	–	16.9	21.4	4.5
Linear strain	(4×4)	+2.5%	1.7	16.7	21.3	4.6
(uniaxial)	(4×4)	+5%	6.3	16.5	21.1	4.6
	(4×4)	+7.5%	13.4	16.3	21.0	4.7
	(4×4)	+10%	22.8	16.2	20.8	4.6
Areal strain	(4×4)	+2.5%	3.8	16.6	21.2	4.6
(biaxial)	(4×4)	+5%	14.2	16.1	20.7	4.6
	(4×4)	+7.5%	29.8	15.8	20.4	4.6
	(4×4)	+10%	49.6	15.5	20.1	4.6

best structural candidates for improvement are the concave sites in rippled graphene geometries, and Stone-Wales defect sites. If these features can be deliberately introduced, then enhancements of 20–30% in binding strength can be expected, translating to commensurately higher storage capacity. However, we caution that our results should be considered as an initial guide, and appropriate classical force-fields will have to be developed to examine the implications of our findings on binding and gas separations at finite temperature and pressure.

V. ACKNOWLEDGMENTS

We acknowledge funding from Bharat Petroleum Corporation Limited (BPCL), India. Helpful conversations with G. Vasudev, N. V. Choudary and B. Newalkar of BPCL, India are gratefully acknowledged. BW was funded by the National Science Foundation Grant 701180. Computations were performed using the facilities of the Centre for Computational Materials Science, Jawaharlal Nehru Centre for Advanced Scientific Research, Jakkur, India. A portion of this work was performed under the auspices of the U.S. Department of Energy by Lawrence Livermore National Laboratory under Contract DE-AC52-07NA27344.

[1] V. Menon and S. Komarneni, Journal of Porous Materials **5**, 43 (1998).
[2] R. E. Morris and P. S. Wheatley, Angew. Chem. Intl. Ed. **47**, 4966 (2008).
[3] J. Schrier, ACS Appl. Mater. Interfaces **3**, 4451 (2011).
[4] A. Celzard and V. Fierro, Energy and Fuels **19**, 573 (2005).
[5] B. C. Wood, S. Y. Bhide, D. Dutta, V. S. Kandagal, A. D. Pathak, S. N. Punnathanam, K. G. Ayappa, and S. Narasimhan, J. Chem. Phys. **137**, 054702 (2012).
[6] V. S. Kandagal, A. Pathak, K. G. Ayappa, and S. N. Punnathanam, The Journal of Physical Chemistry C **116**, 23394 (2012).
[7] C. E. Wilmer, M. Leaf, C. Y. Lee, O. K. Farha, B. G. Hauser, J. T. Hupp, and R. Q. Snurr, Nature Chemistry **4**, 83 (2012).
[8] D. Lozano-Castello, D. Cazorla-Amores, A. Linares-Solano, and D. Quinn, Carbon **40**, 989 (2002).
[9] T. Duren, L. Sarkisov, O. M. Yaghi, and R. Q. Snurr, Langmuir **20**, 2683 (2004).
[10] F. Banhart, J. Kotakoski, and A. V. Krasheninnikov, ACS Nano **5**, 26 (2011).
[11] E.-A. Kim and A. H. C. Neto, Europhys. Lett.) **84**, 57007 (2008).
[12] P. J. F. Harris, Z. Liu, and K. Suenaga, J Phys. Condens. Mat. **20**, 362201 (2008).
[13] S. Sircar, T. C. Golden, and M. B. Rao, Carbon **34**, 1 (1996).
[14] H. Kabbour, T. F. Baumann, J. H. Satcher, A. Saulnier, and C. C. Ahn, Chem. Mater. **18**, 6085 (2006).
[15] J. Biener, M. Stadermann, M. Suss, M. A. Worsley, M. M. Biener, K. A. Rose, and T. F. Baumann, Energy Environ. Sci. **4**, 656 (2011).
[16] J. Kotakoski, A. V. Krasheninnikov, U. Kaiser, and J. C. Meyer, Phys. Rev. Lett. **106**, 105505 (2011).
[17] J. Biener, S. Dasgupta, L.-H. Shao, D. Wang, M. A. Worsley, A. Wittstock, J. R. Lee, M. M. Biener, C. Orme, S. O. Kucheyev, et al., Adv. Mater. **24**, 5083 (2012).
[18] A. H. Castro Neto, F. Guinea, N. M. R. Peres, K. S. Novoselov, and A. K. Geim, Rev. Mod. Phys. **81**, 109 (2009).
[19] P. Giannozzi *et al.*, J. Phys. Condens. Mat. **21**, 395502 (2009).
[20] N. Marzari, D. Vanderbilt, A. D. Vita, and M. C. Payne, Phys. Rev. Lett. **82**, 3296 (1999).

[21] T. Thonhauser, V. R. Cooper, S. Li, A. Puzder, P. Hyldgaard, and D. C. Langreth, Phys. Rev. B **76**, 125112 (2007).

[22] M. Dion, H. Rydberg, E. Schröder, D. C. Langreth, and B. I. Lundqvist, Phys. Rev. Lett. **92**, 246401 (2004).

[23] Y. Zhang and W. Yang, Phys. Rev. Lett. **80**, 890 (1998).

[24] A. Hashimoto, K. Suenaga, A. Gloter, K. Urita, and S. Iijima, Nature **430**, 870 (2004).

[25] M. H. Gass, U. Bangert, A. L. Bleloch, P. Wang, R. R. Nair, and A. K. Geim, Nat. Nanotechnol. **3**, 676 (2008).

[26] J. C. Meyer, C. Kisielowski, R. Erni, M. D. Rossell, M. F. Crommie, and A. Zettl, Nano Lett. **8**, 3582 (2008).

[27] J. H. Warner, M. H. Rümmeli, L. Ge, T. Gemming, B. Montanari, N. M. Harrison, B. Büchner, and G. A. D. Briggs, Nat. Nanotechnol. **4**, 500 (2009).

[28] C. O. Girit, J. C. Meyer, R. Erni, M. D. Rossell, C. Kisielowski, L. Yang, C.-H. Park, M. F. Crommie, M. L. Cohen, and S. G. Louie, Science **323**, 1705 (2009).

[29] M. M. Ugeda, I. Brihuega, F. Guinea, and J. M. Gómez-Rodrguez, Phys. Rev. Lett. **104**, 096804 (2010).

[30] L. Tapasztó, G. Dobrik, P. Nemes-Incze, G. Vertesy, P. Lambin, and L. P. Biró, Phys. Rev. B **78**, 233407 (2008).

[31] J. A. Rodríguez-Manzo, O. Cretu, and F. Banhart, ACS Nano **4**, 3422 (2010).

[32] J. Lahiri, Y. Lin, P. Bozkurt, I. I. Oleynik, and M. Batzill, Nat. Nanotechnol. **5**, 326 (2010).

[33] P. Lehtinen, A. Foster, Y. Ma, A. Krasheninnikov, and R. Nieminen, Phys. Rev. Lett. **93**, 187202 (2004).

[34] A. V. Krasheninnikov and F. Banhart, Nat. Mater. **6**, 723 (2007).

[35] A. Bagri, C. Mattevi, M. Acik, Y. J. Chabal, M. Chhowalla, and V. B. Shenoy, Nat. Chem. **2**, 581 (2010).

[36] B. Sanyal, O. Eriksson, U. Jansson, and H. Grennberg, Phys. Rev. B **79**, 113409 (2009).

[37] Y. Liu and J. Wilcox, Environ. Sci. Tech. **45**, 809 (2011).

[38] J. C. Meyer, C. O. Girit, M. F. Crommie, and A. Zettl, Nature **454**, 319 (2008).

[39] J. A. Vergés and P. L. de Andres, Phys. Rev. B **81**, 075423 (2010).

[40] A. Allouche and Y. Ferro, Carbon **44**, 3320 (2006).

[41] L. Huang, L. Zhang, Q. Shao, L. Lu, X. Lu, S. Jiang, and W. Shen, The Journal of Physical Chemistry C **111**, 11912 (2007).

[42] E. D. Biase and L. Sarkisov, Carbon pp. – (2013), ISSN 0008-6223, URL `http://www.sciencedirect.com/science/article/pii/S0008622313006957`.

[43] L. Li, S. Reich, and J. Robertson, Phys. Rev. B **72**, 184109 (2005).

[44] J. Ma, D. Alfè, A. Michaelides, and E. Wang, Phys. Rev. B **80**, 033407 (2009).

[45] J. Červenka, M. I. Katsnelson, and C. F. J. Flipse, Nature Phys. **5**, 840 (2009).

[46] J. Červenka and C. Flipse, Phys. Rev. B **79**, 195429 (2009).

[47] Z. Liu, K. Suenaga, P. J. F. Harris, and S. Iijima, Phys. Rev. Lett. **102**, 015501 (2009).

[48] O. Cretu, A. V. eninnikov, J. A. Rodríguez-Manzo, L. Sun, R. M. Nieminen, and F. Banhart, Phys. Rev. Lett. **105**, 196102 (2010).

[49] P. L. de Andres and J. A. Vergés, Appl. Phys. Lett. **93**, 171915 (2008).

[50] F. Atamny, T. F. Fässler, A. Baiker, and R. Schlögl, Applied Physics A **71**, 441 (2000).

[51] F. Atamny, A. Baiker, and R. Schlogl, Fresenius J Anal Chem **358**, 344 (1997).

[52] S. Park, D. Srivastava, and K. Cho, Nano Letters **3**, 1273 (2003).

[53] B. Zhou, W. G. Guo, and C. Tang, Nanotechnology **19**, 075707 (2008).

[54] K. Kim, Z. Lee, B. D. Malone, K. T. Chan, B. Alemán, W. Regan, W. Gannett, M. F. Crommie, M. L. Cohen, and A. Zettl, Phys. Rev. B **83**, 245433 (2011).

[55] Y. Takagi and S. Okada, J. Phys. Soc. Jpn. **79**, 033702 (2010).

[56] B. C. Wood, T. Ogitsu, M. Otani, and J. Biener, submitted (2013).